Year: 2024

Myelin bilayer mapping in the human brain in vivo

Baadsvik, Emily Louise ; Weiger, Markus ; Froidevaux, Romain ; Schildknecht, Christoph Michael ; Ineichen, Benjamin Victor ; Pruessmann, Klaas Paul

Magnetic Resonance in Medicine

Myelin bilayer mapping in the human brain in vivo

Emily Louise Baadsvik[1] | **Markus Weiger[1]** | **Romain Froidevaux[1]** |
Christoph Michael Schildknecht[1] | **Benjamin Victor Ineichen[2,3]** |
Klaas Paul Pruessmann[1]

[1]Institute for Biomedical Engineering, ETH Zurich and University of Zurich, Zurich, Switzerland

[2]Department of Neuroradiology, Clinical Neuroscience Center, University Hospital Zurich, University of Zurich, Zurich, Switzerland

[3]Center for Reproducible Science, University of Zurich, Zurich, Switzerland

Correspondence
Markus Weiger, Institute for Biomedical Engineering, ETH Zurich and University of Zurich, 8092 Zurich, Switzerland.
Email: weiger@biomed.ee.ethz.ch

Abstract

Purpose: To quantitatively map the myelin lipid-protein bilayer in the live human brain.

Methods: This goal was pursued by integrating a multi-TE acquisition approach targeting ultrashort T_2 signals with voxel-wise fitting to a three-component signal model. Imaging was performed at 3 T in two healthy volunteers using high-performance RF and gradient hardware and the HYFI sequence. The design of a suitable imaging protocol faced substantial constraints concerning SNR, imaging volume, scan time, and RF power deposition. Model fitting to data acquired using the proposed protocol was made feasible through simulation-based optimization, and filtering was used to condition noise presentation and overall depiction fidelity.

Results: A multi-TE protocol (11 TEs of 20–780 μs) for in vivo brain imaging was developed in adherence with applicable safety regulations and practical scan time limits. Data acquired using this protocol produced accurate model fitting results, validating the suitability of the protocol for this purpose. Structured, grainy texture of myelin bilayer maps was observed and determined to be a manifestation of correlated image noise resulting from the employed acquisition strategy. Map quality was significantly improved by filtering to uniformize the k-space noise distribution and simultaneously extending the k-space support. The final myelin bilayer maps provided selective depiction of myelin, reconciling competitive resolution (1.4 mm) with adequate SNR and benign noise texture.

Conclusion: Using the proposed technique, quantitative maps of the myelin bilayer can be obtained in vivo. These maps offer unique information content with potential applications in basic research, diagnosis, disease monitoring, and drug development.

KEYWORDS
high-performance gradient, HYFI, noise correlation, quantitative mapping, ultrashort-TE

1 | INTRODUCTION

Myelin is an insulating layer surrounding axons that facilitates efficient transmission of neuronal impulses. Myelin is a chief constituent of white matter (WM) but can be found to a lesser extent also in gray matter (GM).[1] Myelin abnormalities, specifically the loss of myelin (demyelination) or errors in myelin development, are associated with clinical disability and feature in many neurological disorders, most prominently multiple sclerosis.[2,3] To monitor the progression of myelin disorders, study the involved pathomechanisms, or assess the impact of therapies aimed at regenerating myelin, techniques for noninvasive, quantitative mapping of myelin are warranted. An established technique for myelin imaging, known as myelin water imaging,[4] targets water trapped within the myelin sheath and yields a versatile measure of myelin content.[5]

Another strategy is to target the macromolecular structure of the myelin sheath, namely the lipid-protein bilayer. A key challenge for visualization of the myelin bilayer is the extremely rapid decay of resonance signals stemming from this structure; about 75% of the signals exhibit T_2s below $100\,\mu s$.[6] This challenge is addressed by dedicated short-T_2 imaging techniques[7] that, in conjunction with specialized RF and gradient hardware, have enabled signals with T_2s down to $10\,\mu s$ to be imaged at high resolution.[8] Recently, the same imaging system was used for quantitative mapping of the myelin bilayer in ex vivo brain tissue,[6,9] which was achieved by fitting a three-component signal model to a multi-TE image series to isolate the contributions of myelin bilayer signals. The maps demonstrated sensitivity to myelin pathology and high specificity for myelin.[10] These properties would be valuable to study the live brain, calling for an in vivo technique with the same functionality.

Expansion of the myelin bilayer mapping technique to in vivo application faces substantial technical hurdles related to imaging a volume orders of magnitude larger within comparable scan time while adhering to safety regulations restricting RF power deposition (quantified by the specific absorption rate [SAR]). In the ex vivo experiments, single-point imaging (SPI),[11] in which pure phase encoding is used to sample each k-space point at the same time after RF excitation,[12,13] was used to achieve a favorable point spread function (PSF) and unbiased fitting results. However, SPI is far too time consuming, SAR intensive, and SNR inefficient for use in vivo.

High sampling efficiency for short-T_2 imaging can be attained using radial, center-out readouts for which gradient ramping is completed before RF excitation to achieve maximum encoding speed.[14–16] With this ramp-first sequence design, the center of k-space is met at time zero (i.e., the magnetic center of the RF pulse). That said, the RF system requires a finite time, known as the dead-time (DT), until the onset of data acquisition, which translates to a data gap in central k-space. Small gaps can be filled by finite extrapolation,[15] but larger gaps must be filled by additional acquisitions at reduced gradient strength.

Two main sampling strategies exist for filling the gap: SPI acquisitions, as in the pointwise encoding time reduction with radial acquisition (PETRA)[16] technique, or radial readouts, as in the water-suppressed and fat-suppressed proton projection (WASPI)[14] technique. In the hybrid filling (HYFI)[17] technique, the gap is filled with a flexible combination of SPI and radial readouts, which offers high sampling efficiency without significantly compromising PSF integrity through T_2 modulation; this technique has already shown promise for short-T_2 brain imaging in vivo.[6] As such, HYFI is considered a viable prospect for in vivo myelin bilayer mapping but poses considerable challenges that must be handled.

First, targeting short-T_2 signals with high imaging and excitation bandwidths, as in the ramp-first sequence design, implies low base SNR and operation at the SAR limit. Combined with constraints on scan time and spatial resolution, these characteristics conflict with the necessity for a multi-TE protocol that produces data with sufficient information content for successful model fitting. Second, radial readouts introduce time evolution across k-space, which complicates the definition of TE for the fitting procedure because the images do not accurately represent the signal state at discrete time points. Finally, nonuniform sampling, as performed in HYFI, is expected to be reflected in noise behavior, which may prove critical at low SNR.

In this work, these challenges are addressed to develop a procedure for in vivo myelin bilayer mapping. Specifically, a HYFI-based multi-TE protocol that adheres to applicable safety regulations while meeting practical scan time limits is constructed. The suitability of data acquired using this protocol for the model fitting procedure is investigated and optimized through simulations, and filtering is used to condition noise presentation and overall depiction fidelity. Moreover, basic tissue segmentation is performed to inspect component amplitudes in WM and GM.

2 | METHODS

2.1 | General setup

Dedicated short-T_2 methodology and hardware are necessary to achieve early detection and rapid spatial encoding of myelin bilayer signals. To this end, a 3T Philips Achieva (Philips Healthcare, the Netherlands) system equipped with a custom-built gradient capable of over

T A B L E 1 Parameters of the multi-TE HYFI imaging protocol with 3D isotropic geometry.

FOV [mm]	Δr [mm]	TR [ms]	RF pulse	Scan time [min:s]	Gap [dw]	HYFI-A
General						
260	1.40	2.1	8 µs 1.7° FA	4:47 per NSA	34	0.11
TE [µs]	**BW [kHz]**	**G_{max} [mT/m]**	**HYFI-T_2 [µs]**	**NSA**		
Multi-TE series						
20	1700	154	20	5		
26	1360	123	25	3		
41	850	77	40	2		
62	566	51	60	1		
93	377	34	90	1		
145	242	22	140	1		
206	170	15	200	1		
290	121	11	280	1		
414	85	8	400	1		
570	62	6	550	1		
776	45	4	750	1		

Abbreviations: BW, image bandwidth; FA, flip angle; gap, radius of the DT data gap (in Nyquist dwells, dw); G_{max}, maximum gradient strength; HYFI-A, HYFI amplitude factor; HYFI-T_2, HYFI target T_2; NSA, number of signal averages; Δr, nominal resolution.

200 mT/m gradient strength at 100% duty cycle,[18] a ^{1}H-free transmit/receive quadrature birdcage coil,[19] and a dedicated RF chain[20] including fast, high-power transmit/receive switches (switching time <1 µs) was used.[21]

The heads of two healthy males aged 52 and 54 years were imaged: Data from one of the volunteers are used for technique development and demonstration in the main manuscript, and data from the other volunteer are included as Supporting Information as a preliminary test of technique reproducibility. Written informed consent was obtained, and the study conformed with regional ethics regulations. An inflatable head support (CRANIA, Pearl Technology, Switzerland) was used for motion reduction and volunteer comfort.

2.2 | Protocol development

The radius of the data gap in central k-space characteristic to the ramp-first sequence design, measured in Nyquist dwells, is given by

$$\text{gap} = \text{DT} \times \text{BW}, \qquad (1)$$

where BW is the image bandwidth, which is proportional to the gradient strength.

In HYFI, the TE is closely linked to the DT. The minimum, technical DT is fixed for a given system configuration; however, to increase TE, it is possible to deliberately prolong the DT by delaying the onset of data acquisition beyond the minimum DT. At fixed BW, increasing the DT leads to an increased gap. For the multi-TE protocol, the radius of the gap was kept constant to maintain a consistent k-space pattern by varying the BW between images according to Eq. (1). The longer readout durations resulting from reduced BWs were accepted because at longer DTs, signals with relatively short T_2s have largely died out and, as such, are not expected to cause problems related to apodization.

The exact distribution of Cartesian SPI and radial acquisitions for a given HYFI scheme is determined by how much signal decay is permitted within the gap, which is controlled by the amplitude factor (HYFI-A) and target T_2 (HYFI-T_2). The amount of permitted decay corresponds to a maximum time after the DT during which data are sampled, defined as

$$T_{acq} = (-\text{HYFI-}T_2) \times \ln(1 - \text{HYFI-A}) \qquad (2)$$

A larger T_{acq} results in fewer SPI acquisitions and longer radial readouts, which leads to shorter scan times but increases exposure to signal decay, potentially causing artifacts. That said, it is reasonable to use a larger T_{acq} for images with a longer DT because relatively short-lived signals will have already died out. For this reason,

HYFI-A was kept constant and HYFI-T_2 was set equal to the DT.

An overview of the multi-TE protocol is provided in Table 1. The protocol has 3D isotropic geometry and consists of 11 HYFI images at TEs from 20 to 780 μs with a nominal resolution of 1.4 mm. The main radial readouts were extended to explore the feasibility of using the full k-space extent available within the given sequence timing, resulting in angular undersampling by a factor of 1.5 outside the gap.[22] The total scan time was 1.5 h. Images with higher BWs have proportionally lower SNR due to their faster readouts, so corresponding signal averaging was performed to reach an acceptable SNR in all images. The same excitation pulse was used for all images to achieve the same flip angle. The pulse was frequency-swept and optimized over the BW of the TE_{min} image.[23]

The acquisition scheme of the protocol, represented by the time evolution across k-space, is illustrated in Figure 1. The innermost k-space is sampled using SPI, and the remainder of the gap is sampled using a series of radial acquisitions at increasing gradient strength. Outside the gap, a radial acquisition at full gradient strength is performed. Note that filling the gap entirely using SPI (i.e., setting HYFI-A = 0), as in the PETRA technique, would increase the scan time by 60%.

2.3 | Fitting procedure

To isolate the contributions from the myelin bilayer, a three-component signal model derived from human WM ex vivo[9] was fitted to the multi-TE HYFI image series using a least-squares algorithm. Two of the components represent nonaqueous protons and are characterized by super-Lorentzian lineshapes,[24,25] which correspond to a characteristic spectrum of T_2s represented by the minimum decay component, $T_{2,min}$ (note that measured signals technically decay by T_2^*, but decay constants are denoted by T_2 throughout this work because T_2' is considered negligible). Of the two nonaqueous components, one is described by an ultrashort $T_{2,min}$ of 5.5 μs and a chemical shift of 1.1 ppm, whereas the other is described by a short $T_{2,min}$ of 100 μs and a chemical shift of 2.1 ppm. The ultrashort (U) component is interpreted as representing the myelin bilayer, and the short (S) component is interpreted as representing residual short-T_2 content such as nonmyelin cell membranes or proteins. The remaining (W) component represents water signals and is characterized by a Lorentzian lineshape with a T_2 of 50 ms and a chemical shift of 4.7 ppm.

The fitting procedure was applied on a voxel-by-voxel basis, thereby producing maps of each free model

parameter. The parameters determined by the fit were the amplitudes of each of the signal components (A_U, A_S, and A_W), an arbitrary phase offset (φ), and a local resonance frequency offset (Δf).

The fitting procedure requires each image to be assigned a single time value (i.e., the TE) representing the state of the underlying signals. However, it is clear from Figure 1 that HYFI images contain contributions from a distribution of points on the time evolution of the measured signals; as such, it is unclear how TE should be defined. Given the dominance of central k-space with regard to signal intensity, TE was defined as

$$TE = DT + \lambda\, T_{acq}, \tag{3}$$

where λ is an arbitrary scaling factor. For the protocol used in this work, an optimal value for λ was determined empirically through simulations (λ = 0.31; see Section 3).
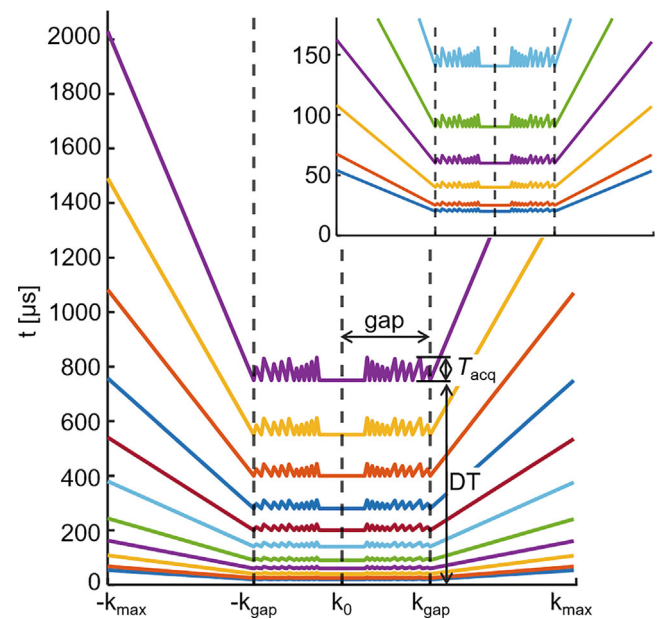

FIGURE 1 k-Space acquisition scheme of the multi-TE HYFI protocol. The time elapsed after the magnetic center of the RF pulse is plotted as a function of k-space position. The displayed 1D pattern is symmetric throughout 3D k-space. For radial acquisitions, the gradient strength is proportional to the inverse of the slope. The DT and T_{acq} are illustrated for the TE_{max} (equivalent to DT_{max}) image. Note that for an equivalent SPI protocol, the acquisition scheme would correspond to horizontal lines at the DTs. k_{max} denotes the maximum k-space extent from the k-space center, k_0, and k_{gap} denotes the k-space extent of the DT data gap. The inlet contains a magnified view of the shortest TEs. Notably, the k-space gap has the same size for all TEs, and the HYFI scheme inside the gap is matched across TEs.

2.4 | Image subtraction

For comparison with the previously presented HYFI-based approach for in vivo short-T_2 brain imaging,[6] the magnitude of the TE_{max} image was subtracted from the magnitude of the TE_{min} image to produce a subtraction image in which the contributions from aqueous signals are suppressed. Consequently, the subtraction image is dominated by nonaqueous contributions.

2.5 | Anatomical reference image

A T_1-weighted 3D gradient echo image (TR = 10 ms, TE = 3.65 ms, flip angle = 15°) with the same FOV and resolution as the HYFI data was acquired for anatomical reference using the standard configuration of the 3T Philips Achieva system (i.e., commercial gradient and RF chain) and a Philips 8-channel receive-only head array.

2.6 | Image processing

The complex HYFI images were reconstructed separately for the two channels of the birdcage coil and subsequently quadrature-combined. To correct for subject motion, individual signal averages were 3D rigid-body-registered before combination, and the combined images were registered to each other. The final images were bias-corrected.[26] The T_1-weighted anatomical reference image was registered to the processed HYFI images through a 3D affine transformation and bias-corrected. All image registrations were performed using *MATLAB* (MathWorks, Natick, MA, USA) inbuilt functions.

All images were interpolated to three times the original matrix size for display. For fitted maps and the subtraction image, three slices (in the through-slice direction) were averaged to increase the SNR for display unless otherwise stated.

The impact of the acquisition scheme on noise presentation and depiction fidelity was investigated by applying reconstruction filters that attenuate different parts of k-space. Two filters were explored, as well as two reconstruction matrix sizes (see Figure 5B). Each filter/matrix combination was applied to the full multi-TE image series to produce a total of five reconstruction cases: Three cases use an isotropic matrix size $M = 152$ (corresponding to full Nyquist sampling and a nominal resolution of 1.7 mm) with either no filter, a hyperbolic secant filter[27] with exponent 10 and truncation factor 5, or a cosine filter of periodicity $2M$; and the remaining two cases use the nominal matrix size $M = 186$ with either no filter or a cosine filter of periodicity $2M$. The reconstruction case producing the

highest quality myelin bilayer map was determined and used throughout the remainder of this work ($M = 186$ with the cosine filter; see Section 3).

2.7 | Simulations

The impact on the model fitting procedure of using HYFI data was investigated through 3D simulations. The signal model described for data fitting was used to generate the simulated signals, and the amplitudes of the U-component, S-component, and W-component were set to 0.40, 0.05 and 0.55, respectively, in accordance with values reported for human WM ex vivo.[9] The simulated object was an off-centered sphere with diameter spanning 60% of the FOV. The same HYFI protocol as used in vivo (see Table 1) was used. For reference, an equivalent protocol (i.e., identical DTs) with purely SPI acquisitions was also used.

The simulation did not include the effects of noise, no filtering was performed, and the simulated data were fitted using the same signal model as was used to generate the data. Consequently, the component amplitudes fed into the simulation form the ground truth for the model fitting procedure.

For fitting of the simulated SPI data, the TEs were set equal to the DTs. For the simulated HYFI data, different TE schemes were used, corresponding to different values of λ (see Eq. [3]).

Further simulations to establish the stability of the fitting procedure in the presence of noise can be found in Supporting Information Part 1.

2.8 | Tissue segmentation

The amplitudes of the signal components were collected for a large number of voxels of either WM or GM to estimate the contributions of each component in the two tissue types. Basic threshold-based image segmentation was performed (using *MATLAB* inbuilt functions) on the anatomical reference image for 15 axial slices in which WM and GM were clearly differentiated. The WM mask was eroded to avoid voxels at risk of partial volume, but such processing was not possible on the GM mask due to the low thickness of GM structures.

3 | RESULTS

For the simulated data used to probe the impact of the acquisition scheme on the model fitting procedure, the means and SDs of the fitted component amplitudes over
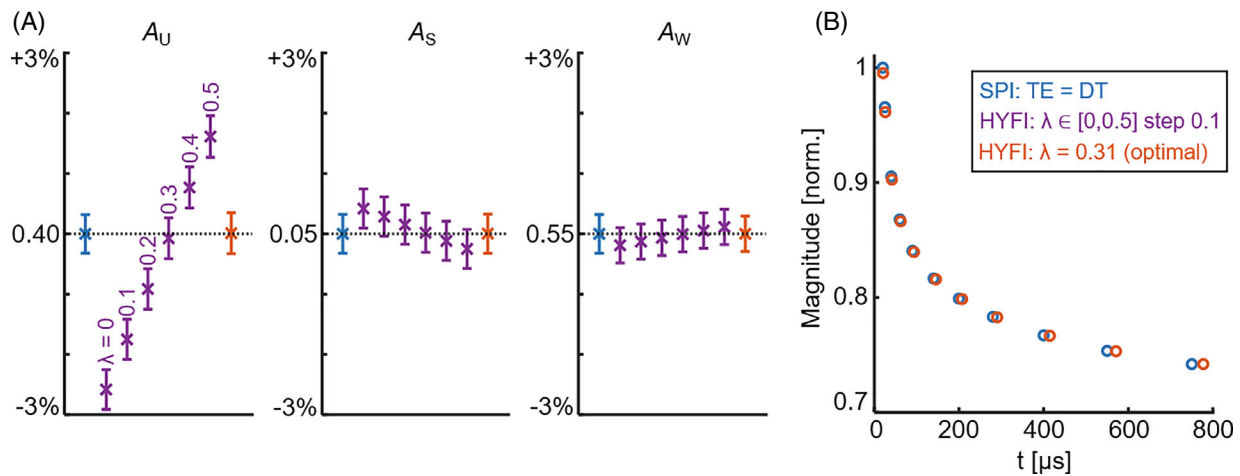
FIGURE 2 Results of the data simulations. (A) Fitted component amplitudes (A_U, A_S, and A_W) averaged over a large number of voxels, with error bars representing the SD, which is non-zero due to effects of the PSFs. The ground truth amplitudes for each component are indicated by dotted black lines. The SPI data return the ground truth amplitudes for all components. For the hybrid filling (HYFI) data, setting $\lambda = 0$ (see Eq. [3]) yields a myelin bilayer component amplitude (A_U) that is lower than the ground truth, but the amplitude is increased by increasing λ; the relationship between the component amplitudes and λ appears linear. The ground truth amplitudes for all three components are recovered by setting $\lambda = 0.31$, making this the optimal value for the employed HYFI protocol. (B) Single-voxel decay curves of the simulated data for HYFI with $\lambda = 0.31$ and SPI. The magnitudes are slightly reduced for the HYFI data compared to the SPI data because the HYFI data experience signal decay across k-space.
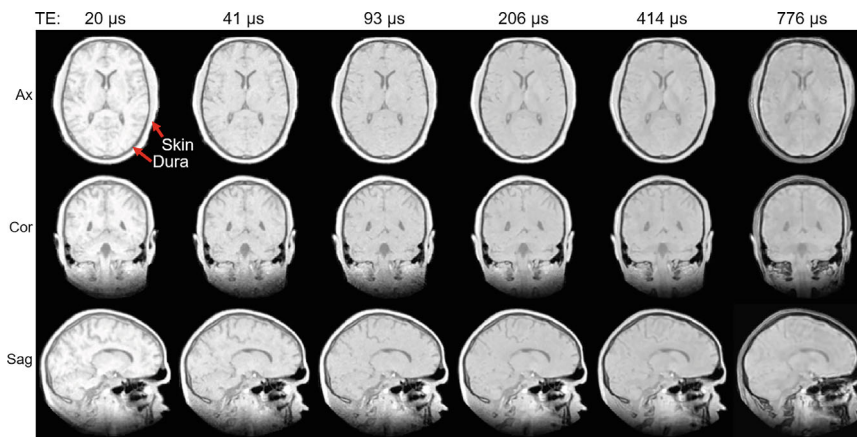

FIGURE 3 Subset of the full multi-TE HYFI image series showing one slice in each 3D orientation. All images use the same intensity scale. The intensity and contrast change with increasing TE, reflecting the decay of short-T_2 signals. All images are masked based on the outline of the head. ax, axial; cor, coronal; sag, sagittal.

a large number of voxels are presented in Figure 2A. As anticipated, the fits to the SPI data returned the ground truth amplitudes. For the HYFI data, setting $\lambda = 0$ produced myelin bilayer amplitudes significantly lower than the ground truth, indicating that the TEs are too short in this scheme. Increasing λ up to $\lambda = 0.5$ produced a practically linear increase in the myelin bilayer amplitudes. The empirically optimized value, $\lambda = 0.31$, returned the ground-truth amplitudes for all components.

The justification for using longer TEs for HYFI compared with SPI data is illustrated in Figure 2B, which shows single-voxel decay curves for the simulated data. The HYFI data exhibit lower magnitudes than the SPI data because HYFI experiences signal decay across k-space (see Figure 1). For the SPI and HYFI data to reflect the same

underlying signals (i.e., for the decay curves to be equivalent), the HYFI data must represent later sampling times.

A subset of the in vivo multi-TE image series is presented in Figure 3, demonstrating signal decay and changes in tissue contrast at longer TEs. As the TEs increase, WM darkens relative to GM, the layer of skin around the head loses intensity, the signals from the dura (a thin layer of dense connective tissue around the brain) decay away, and CSF intensity tends to increase because the spoiling effect of the gradient decreases.[28] The image quality is generally good, although the effects of rather low SNR can be observed for the shorter TEs. No undersampling artifacts are apparent.

Figure 4 contains an example fit to the multi-TE data from a single WM voxel. The magnitude decays rapidly
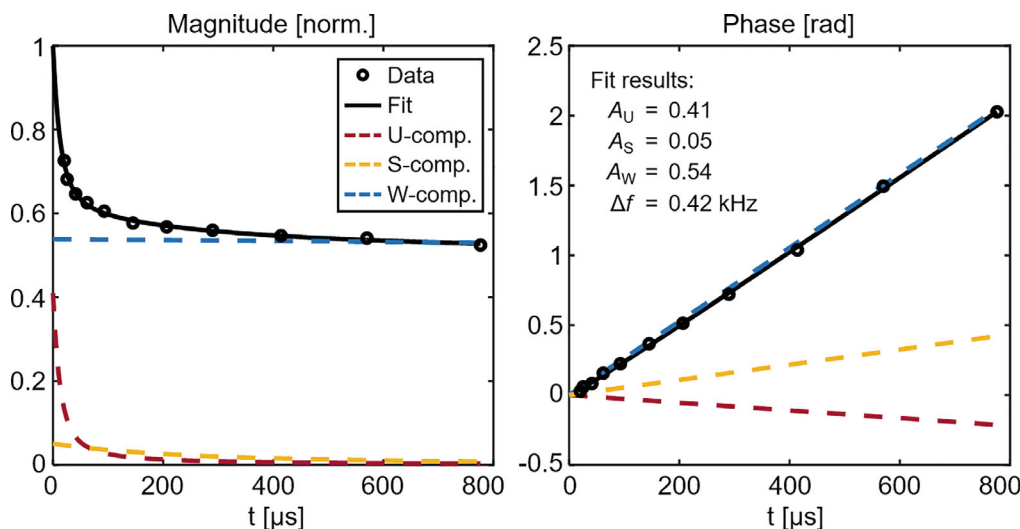
FIGURE 4 Example fit to the multi-TE data in a single WM voxel. The magnitude (left) and phase (right) evolution of the data are presented together with the fitting results, including the contributions of each signal component. The magnitude exhibits rapid initial decay associated with the contribution of the myelin bilayer (U) component, followed by less rapid decay associated with the contribution of the residual short-T_2 (S) component, before converging to the water level (the amplitude of the W-component). The phase evolution is approximately linear, reflecting the dominant contribution of water signals; the gradient of this line reflects the local resonance frequency offset (Δf). The magnitude was normalized by the sum of the component amplitudes, and the phase was shifted to originate at zero.

at the shortest TEs, reflecting the myelin bilayer component, before transitioning to less rapid decay at intermediate TEs, reflecting the residual short-T_2 component, and finally converging to the water level at the longest TEs. The phase is approximately linear due to the dominant contribution of water signals: the nonaqueous components decay too rapidly for their chemical shifts to affect the signal phase significantly.[9] The fit quality is generally good, with the signal model describing the course of the measured data well.

Fitted amplitude maps of the myelin bilayer component for the five reconstruction cases used to probe the impact of the acquisition scheme on noise presentation and depiction fidelity are shown in Figure 5A. For the Nyquist matrix size ($M = 152$) and no filter, the myelin bilayer map exhibits a structured, grainy texture. With the hyperbolic secant filter, the graininess is reduced but still apparent. With the cosine filter, the graininess is barely noticeable; however, the effective spatial resolution is reduced due to the strong attenuation of outer k-space. The resolution is largely recovered using the nominal matrix size ($M = 186$), which, in conjunction with the cosine filter, yields the highest depiction quality of the explored cases; hence, this reconstruction case was used throughout the remainder of this work. Using the nominal matrix size with no filter produces strong graininess, which indicates that filtering is the main determinant of depiction quality. The impact of the filter on map texture is not related to its standard smoothing effect because the improvements are retained at the nominal

matrix size. Moreover, grainy texture is not apparent in the amplitude map of the water component for the case of Nyquist matrix size and no filter (see Supporting Information Part 2), indicating that the underlying effect does not scale with signal amplitude and is not primarily PSF-related.

Comprehensive outputs of the myelin bilayer mapping procedure are presented in Figure 6A. The myelin bilayer (U) component exhibits high amplitudes in WM, low amplitudes in GM, and practically zero amplitudes in CSF. The S-component representing residual short-T_2 content shows no distinction between WM and GM and is relatively uniform but suffers from particularly low SNR. For the water (W) component, WM appears slightly darker than GM, and CSF exhibits significant amplitudes but appears darker than brain tissue due to the lower steady-state magnetization associated with a longer T_1.[9] The inflatable head support (masked in Figure 3) contributes significantly to the myelin bilayer map and partially to the map of the residual short-T_2 content, which is considered reasonable decay behavior for the plastic material. The map of the local resonance frequency offset primarily reflects the lack of shimming, and the map of the phase offset reflects the B_1 phase of the RF coil. The fit residuals quantifying the goodness of fit are uniform in brain tissue, indicating no significant differences in fit performance between WM and GM, but are large outside the brain and generally elevated in CSF, indicating that the signal model does not accurately describe these tissues/-materials. For comparison, Figure 6B contains a dual-TE
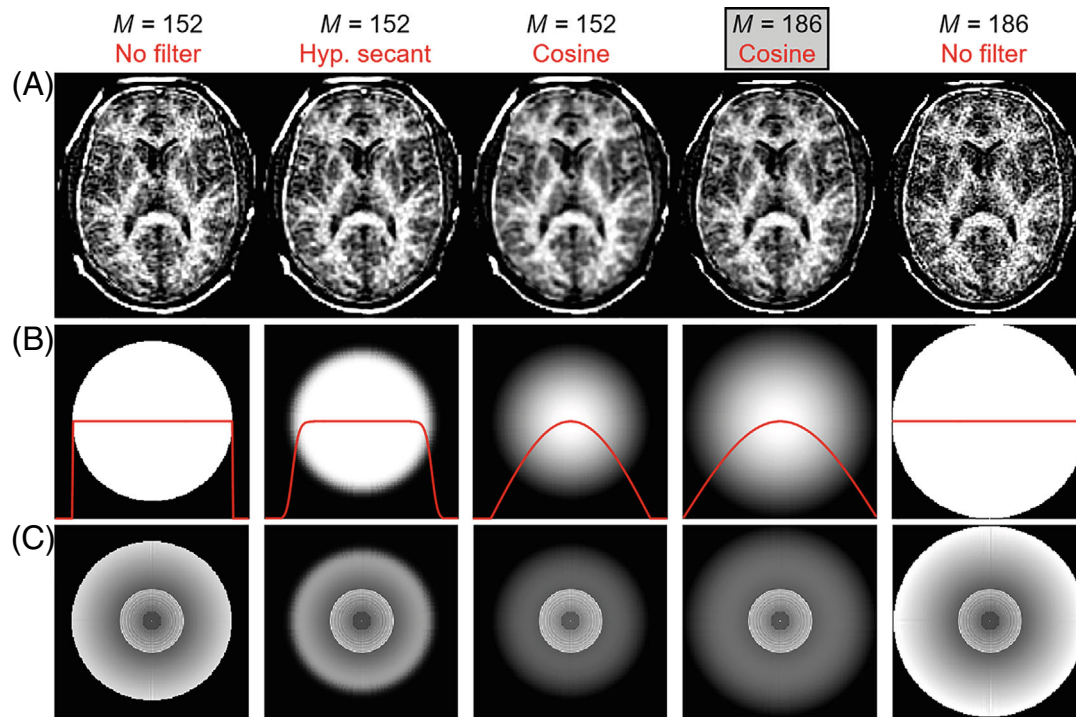
FIGURE 5 (A) Amplitude maps of the myelin bilayer component (A_U) for the axial slice shown in Figure 3 for the five image reconstruction cases. No slice averaging was used. Structured, grainy texture of the maps can be observed, particularly in the front of the brain. The combination of the cosine filter and matrix size $M = 186$ produces the best map quality of the explored cases. (B) Illustration of the respective filters for a central 2D slice from the symmetric 3D k-space, with 1D profiles in red. The difference in k-space support for the two matrix sizes is apparent. (C) Relative noise SD across k-space for the employed acquisition scheme (see Figure 1) for each reconstruction case. Highest uniformity is achieved with the cosine filter. Nonuniform noise across k-space leads to noise correlation in the image domain (see Section 4). The distributions were obtained by gridding the 3D k-space coordinates of the trajectory and computing the inverse square root, followed by application of the respective filter. The display uses a linear intensity scale.
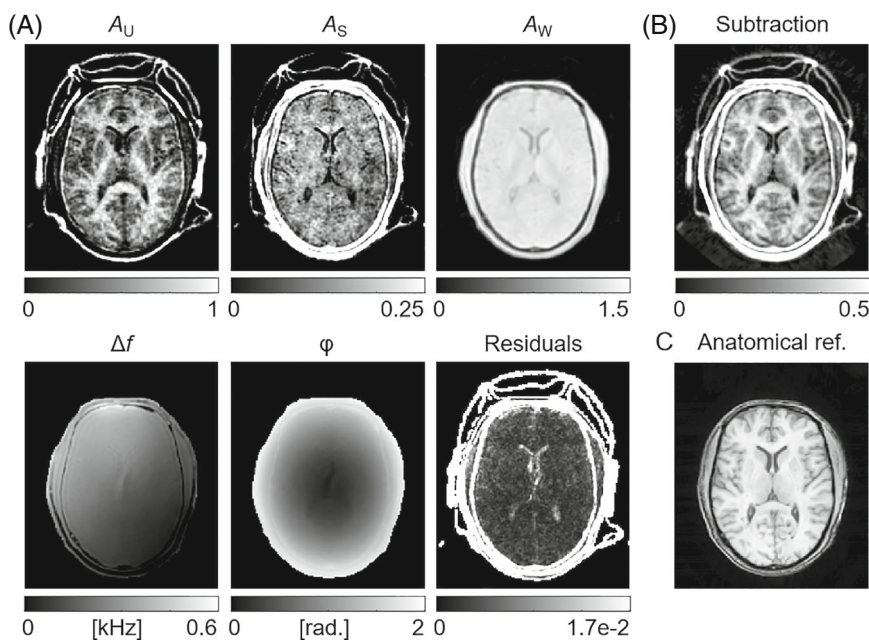

FIGURE 6 Demonstration of the myelin bilayer mapping procedure for the axial slice shown in Figure 3. (A) Maps of the amplitudes of the three signal components (A_U, A_S, and A_W), the local resonance frequency offset (Δf), the phase offset (φ), and the fit residuals quantifying the goodness of fit. (B) Subtraction image (TE_{min}–TE_{max}) for comparison. (C) Anatomical reference image. The outline of the inflatable head support is visible in several of the maps (the Δf and φ maps are masked based on the head outline in the A_W map). The component amplitudes and the magnitude of the subtraction image are directly related, but the image intensities are scaled differently for visualization purposes (see color bars).

TABLE 2 Relative contributions of each signal component in WM and GM.

Tissue	A_U	A_S	A_W
WM	0.35 (0.06)	0.07 (0.02)	0.57 (0.01)
GM	0.21 (0.10)	0.06 (0.03)	0.73 (0.03)

Note: The values represent the means and SDs (in parentheses) of the fitted amplitudes of each signal component across a large number of WM or GM voxels (segmentation masks), normalized by the sum of the mean component amplitudes.

subtraction image and Figure 6C contains an anatomical reference image.

The amplitudes of the signal components averaged over a large number of WM or GM voxels are provided in Table 2. The relative contribution of the myelin bilayer component is significantly larger in WM than in GM (although it should be noted that this component is only considered specific for the myelin bilayer in WM[9]), whereas the fraction of the residual short-T_2 component is similar across the two tissue types. In agreement with the variations observed in the amplitude maps in Figure 6A, the SDs of the GM amplitudes for the nonaqueous components are large. The relative water content is higher in GM than in WM, indicating that differences in proton density outbalance the effects of relatively low T_1 weighting. The ratio of mean absolute WM to GM amplitudes for the water component is 0.96; this value is confirmed by calculations of T_1-weighted steady-state signal levels using T_1s[29] of 832 ms and 1331 ms and water contents[30] of 72% and 82% for WM and GM (assuming equal mass density),[31] respectively.

Figure 7A contains multiple slices from the myelin bilayer map, demonstrating the richness of the data set. Corresponding slices from the anatomical reference image are presented in Figure 7B. The brain stem, cerebellar WM, and corpus callosum are particularly intense in the myelin bilayer map (+15%, +16%, and +3% of the mean amplitude of the myelin bilayer component across the WM segmentation mask, respectively), reflecting the dense myelination of these WM structures. Furthermore, strong contrast is observed between cortical GM (the chief constituent of the GM segmentation mask) and the centrum semiovale (+13% relative to the WM segmentation mask). The myelin bilayer map exhibits low amplitudes in GM structures such as the basal ganglia and thalamus (−28% and +5% relative to the GM segmentation mask, respectively), whereas the anatomical reference image exhibits significantly less contrast between these structures and the surrounding tissue. Similar quality of the myelin bilayer map was found for the other volunteer (see Supporting Information Part 3), demonstrating reproducibility of the technique across individuals.
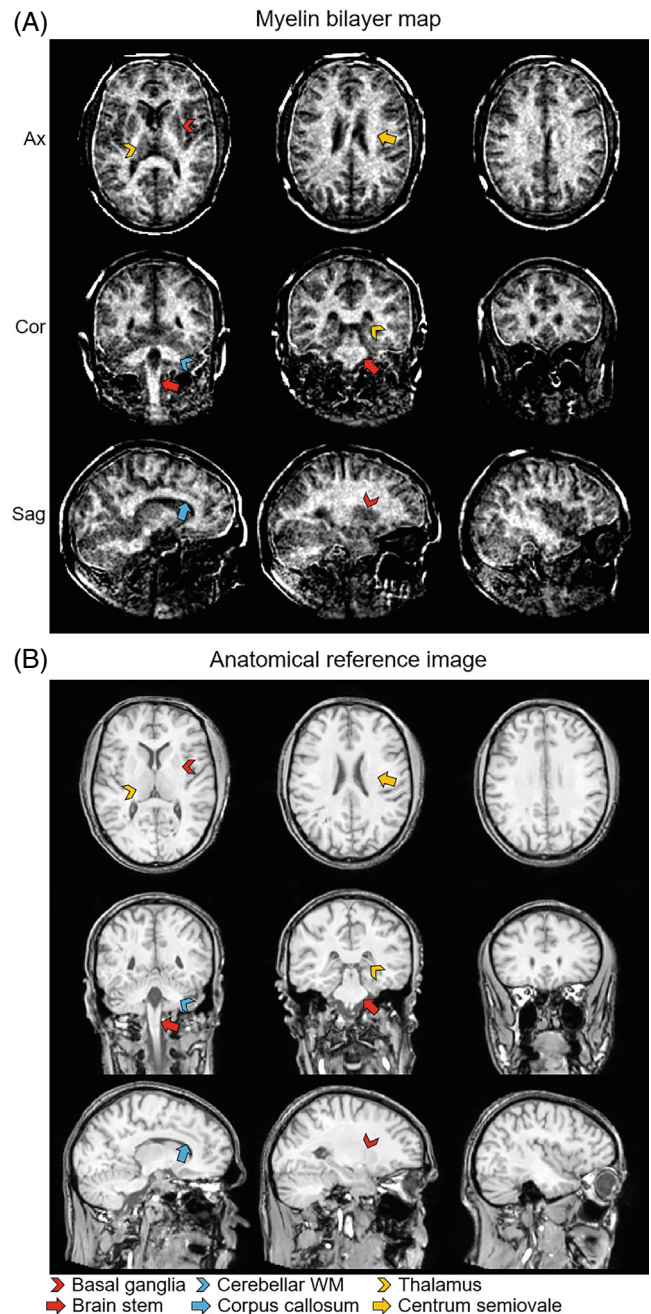

FIGURE 7 (A) Three slices in each 3D orientation from the amplitude map of the myelin bilayer component (A_U). (B) Corresponding slices from the anatomical reference image for comparison. Features of interest are indicated at corresponding locations in the two image types. The leftmost slice for each orientation corresponds to the slices shown in Figure 3. The anatomical reference image extends further down the neck than the myelin bilayer map due to differences in RF coil sensitivities and gradient linearity range. The intermittent outline of the head in the myelin bilayer map reflects contact points between the skin and the inflatable head support. ax, axial; cor, coronal; sag, sagittal.

4 | DISCUSSION

In this exploratory work, an in vivo technique for myelin bilayer mapping in the human head was developed from principles established in ex vivo tissue samples.[6,9,10] Using the proposed technique, quantitative myelin bilayer maps of human brain were obtained in vivo with adequate SNR, resolution, and depiction fidelity.

4.1 | TE definition

The definition of TE is a critical issue for model fitting that was addressed through simulation-based optimization. The results in Figure 2 show that following TE optimization, HYFI data obtained using the proposed protocol yield accurate values for the fitted component amplitudes. This success was contingent on deliberate, joint design of the data-acquisition and TE determination strategies. Using a pure SPI protocol would avoid these considerations but is simply not feasible in vivo: For the simulated SPI protocol with DTs equivalent to those of the HYFI protocol, a maximum gradient strength of over 400 mT/m and a scan time approximately 20 times longer than that of the HYFI protocol would be needed.

The optimal value for λ in Eq. (3) is expected to be protocol dependent and can be obtained using the proposed simulation procedure. For arbitrary HYFI protocols, the TE definition described in Eq. (3) may need to be adjusted.

4.2 | Noise presentation and image quality

The grainy texture of myelin bilayer maps demonstrated in Figure 5A is likely a manifestation of correlated image noise. HYFI acquires k-space with nonuniform acquisition density (i.e., the density of acquired samples along the trajectory resulting from constant acquisition bandwidth, varying gradient strength, and radial geometry), and consequent differences in signal magnitude across k-space are compensated by density correction during image reconstruction. However, after density correction, the noise SD follows the inverse square root of the acquisition density and is nonuniform across k-space (see Figure 5C), which translates to noise correlation in the image domain.[32] The main radial readout (i.e., outside the gap; see Figure 1) has particularly strong influence on the noise distribution because the separation between neighboring spokes increases with k-space radius while the gradient strength remains constant.

The high noise level in outer k-space is particularly critical in 3D because the corresponding volume is relatively large: Two thirds of the noise power sit in the outermost 20% of the k-space radius. As shown in Figure 5C, in the absence of filtering, the noise level is relatively high and its distribution strongly nonuniform, particularly for the nominal matrix size. The hyperbolic secant filter attenuates the outermost k-space, which improves the noise level but does not adequately reduce its nonuniformity. The cosine filter, on the other hand, counteracts the effect of the main radial readout by applying progressively lower weighting for larger k-space radii. This approach substantially reduces the level and nonuniformity of noise outside the gap, thereby reducing noise correlation and overall presence in the image. The impact of filtering on effective spatial resolution can be mitigated by exploiting the full k-space extent afforded by prolonged radial readouts. As evidenced by the results presented in this work, such moderate angular undersampling is benign.

As detailed above, noise correlation is present in any images for which k-space was acquired nonuniformly, but the effects of noise correlation are less noticeable in images with high base SNR (see Supporting Information Part 2). With the intrinsically low SNR of the ramp-first sequence design, acquisition density and compensation strategies are critical aspects in the implementation of such techniques. The cosine filter is an effective solution to reduce noise correlation and power, and major improvements over this strategy are not expected. That said, some further benefit could be gained by designing sequence-aware k-space filters or adapting the imaging sequence to yield a more uniform acquisition density by reducing the gradient strength at larger k-space radii,[33] although this would prolong the readout duration and require more gradient switching.

4.3 | Myelin specificity

High myelin specificity of myelin bilayer maps produced by the three-component fitting procedure was validated by myelin histopathology in ex vivo studies.[9,10] The same methodological principles were implemented for the in vivo technique, and, consequently, the myelin bilayer map presented here is expected to be similarly specific for myelin. This is supported by the equivalence of HYFI and SPI data found in simulations, the overall quality of the fitted maps, and the correspondence between the myelin bilayer map and known myelin distribution of WM and GM structures seen in the anatomical reference image.

As seen in Figure 6A and Table 2, the residual short-T_2 component exhibits nonnegligible amplitudes and is practically uniform across tissues that are known to comprise significantly different proportions of myelin. As such, it

is clear that separating the nonaqueous signals into two components, as achieved here through three-component fitting to multi-TE data, yields improved myelin specificity compared with the dual-TE subtraction approach proposed previously.[6] This effect is evidenced by the subtraction image in Figure 6B exhibiting less contrast between WM and GM than the myelin bilayer map in Figure 6A.

4.4 | Component amplitudes

The relative amplitudes presented in Table 2 for the three signal components across WM and GM correspond well with those reported for ex vivo human brain tissue with native water content.[9] The relative water contents of both tissue types are lower than reported in literature,[30] which can be explained by differences in how the values were obtained; here, the water component amplitudes reflect the combination of water proton density and T_1 weighting, whereas literature values typically reflect mass fractions.

The component amplitude maps in Figure 6 exhibit substantial differences in the non-brain tissues of the head. The signal model was not designed to describe these tissues, but their signals are still sorted into different categories by the fitting procedure. The dura contributes only to the myelin bilayer component, which is reasonable given the extremely rapid decay of highly compact tissues. The strong contributions from the cranium to the residual short-T_2 component likely reflect bone water.[34] Muscle tissue along the temples contributes very slightly to the myelin bilayer component and quite substantially to the residual short-T_2 component, possibly reflecting collagen fibers or muscle cell membranes. The residual short-T_2 component exhibits strong contributions from the scalp, including the skin and subcutaneous connective tissues. It is also worth noting that the myelin bilayer component shows high amplitudes in teeth, which could reflect enamel or collagen.

4.5 | Imaging protocol and practical considerations

Capturing and spatially encoding myelin bilayer signals, with their extremely short T_2s, presents many technical challenges that require both hardware and methodological solutions. The in vivo aspect introduces an additional set of challenges. The ramp-first sequence design requires RF pulses with the same BW as the image to excite the full FOV, which means that high RF power is needed to achieve optimal flip angles. For the current protocol, the optimal flip angle could not be reached due to SAR restrictions. Even for the maximum flip angle permitted by

SAR restrictions, high RF power (approximately 8 kW) was needed, which required a compatible RF chain. Moreover, setting the number and distribution of TEs, the allocation of signal averages, the size of the gap, and the exact HYFI scheme for the protocol was not trivial given the constraints on scan time and data quality; diligent design and testing was required.

The scan time of 1.5 h is at the upper limit of what cooperative volunteers can be expected to manage. For patient studies or testing in larger cohorts, it is desirable to reduce the scan time for increased comfort and overall efficiency. That said, the presented protocol was developed to prove the feasibility of in vivo myelin bilayer mapping and, as such, was not optimized for minimal scan time. Strategies to reduce scan time include reducing the number of TEs, increasing the angular undersampling factor, or modifying the HYFI acquisition scheme, and will require thorough investigation for which the data obtained here form a baseline for comparison. Furthermore, the SNR of the presented protocol is primarily SAR limited, and dedicated optimization could ease this constraint, which in turn could allow for shorter scans. The SNR could also be improved through a more advanced RF coil setup.

Long scan times intensify issues related to subject motion and may require motion correction or compensation strategies beyond the relatively basic approach used here. Common approaches for motion correction[35] are based on intrinsic information,[36] navigator acquisitions, or external sensors. Integration of such methods with HYFI and/or the employed short-T_2 imaging system is feasible, particularly because the requirements for precision and accuracy are moderate at the practicable image resolution.

4.6 | Signal model

The $T_{2,\min}$ values in the signal model were determined for ex vivo WM at room temperature.[9] At body temperature, the decay constants are expected to be somewhat longer (on the order of a few microseconds for the myelin bilayer component and tens of microseconds for the residual short-T_2 component).[37] That said, previous investigations have concluded that differences in the $T_{2,\min}$s on this order do not have much effect on the final results.[9]

The super-Lorentzian lineshape underlying the myelin bilayer signal component assumes a spherical distribution of bilayer segments with respect to the main magnetic field, when, in fact, the distribution of myelin along axons rather takes a cylindrical form. Consequently, it is of interest to explore lineshape models that incorporate cylindrical geometry and account for the orientation of axons.[38]

4.7 | Related techniques

The ultrashort TE (UTE)[39] technique has also been used for short-T_2 brain imaging.[40–48] In UTE, gradient ramping is performed during signal readout, which avoids some of the technical constraints faced by the ramp-first sequence design but limits the achievable spatial encoding speed. Consequently, UTE is primarily sensitive to signals with T_2s in the hundreds of microseconds range, which excludes the majority of myelin bilayer signals.[6] Employing the ramp-first sequence design on an imaging system with standard gradient hardware[49–51] faces similar limitations.

Various MRI techniques to visualize myelin through the detection of water signals exist, which rely mostly on relaxation, magnetization transfer, or diffusion properties.[52,53] By targeting myelin bilayer signals, access to complementary information is gained. Given the key role of the bilayer in the structure and function of the myelin sheath, this information could offer valuable insights regarding myelin development, degeneration, and repair.

5 | CONCLUSIONS

In this work, a technique for in vivo mapping of the myelin bilayer was developed, which produced promising initial results with unique information content. The scan time of the multi-TE protocol represents a barrier to large-scale and patient studies, but further protocol optimization is expected to ease this constraint. Overall, myelin bilayer mapping has the potential to meet the myelin monitoring needs of clinical and research communities, be it for applications in basic research, diagnosis, disease monitoring, or drug development.

CONFLICT OF INTEREST
Klaas Paul Pruessmann holds a research agreement with and receives research support from Philips and is a shareholder of Gyrotools LLC.

ORCID
Emily Louise Baadsvik https://orcid.org/0000-0001-5941-5532
Romain Froidevaux https://orcid.org/0000-0001-7550-5554
Klaas Paul Pruessmann https://orcid.org/0000-0003-0009-8362

REFERENCES
1. Rasband MN, Macklin WB. Myelin structure and biochemistry. In: Brady ST, Siegel GJ, Albers RW, Price DL, eds. *Basic Neurochemistry*. 8th ed/ ed. Elsevier; 2012:180-199.
2. World Health Organization. Neurological disorders: public health challenges. Available at: https://www.who.int/publications/i/item/9789241563369. 2006.
3. Reich DS, Lucchinetti CF, Calabresi PA. Multiple sclerosis. *N Engl J Med.* 2018;378:169-180.
4. MacKay A, Whittall K, Adler J, Li D, Paty D, Graeb D. In vivo visualization of myelin water in brain by magnetic resonance. *Magn Reson Med.* 1994;31:673-677.
5. MacKay AL, Laule C. Magnetic resonance of myelin water: an in vivo marker for myelin. *Brain Plast.* 2016;2:71-91.
6. Weiger M, Froidevaux R, Baadsvik EL, Brunner DO, Rösler MB, Pruessmann KP. Advances in MRI of the myelin bilayer. *Neuroimage.* 2020;217:116888.
7. Weiger M, Pruessmann KP. Short-T_2 MRI: principles and recent advances. *Prog Nucl Magn Reson Spectrosc.* 2019;114-115:237-270.
8. Froidevaux R, Weiger M, Rösler MB, et al. High-resolution short-T_2 MRI using a high-performance gradient. *Magn Reson Med.* 2020;84:1933-1946.
9. Baadsvik EL, Weiger M, Froidevaux R, Faigle W, Ineichen BV, Pruessmann KP. Mapping the myelin bilayer with short-T_2 MRI: methods validation and reference data for healthy human brain. *Magn Reson Med.* 2023;89:665-677.
10. Baadsvik EL, Weiger M, Froidevaux R, Faigle W, Ineichen BV, Pruessmann KP. Quantitative magnetic resonance mapping of the myelin bilayer reflects pathology in multiple sclerosis brain tissue. *Sci. Adv.* 2023;9:eadi0611.
11. Balcom BJ, MacGregor RP, Beyea SD, Green DP, Armstrong RL, Bremner TW. Single-point ramped imaging with T_1 enhancement (SPRITE). *J Magn Reson Ser A.* 1996;123:131-134.
12. Emid S, Creyghton JHN. High resolution NMR imaging in solids. *Physica B+C.* 1985;128:81-83.
13. Mastikhin IV, Balcom BJ. Centric SPRITE MRI of biomaterials with short T_2*. *eMagRes.* 2012;1:783-788.
14. Wu YT, Dai GP, Ackerman JL, et al. Water- and fat-suppressed proton projection MRI (WASPI) of rat femur bone. *Magn Reson Med.* 2007;57:554-567.
15. Weiger M, Pruessmann KP. MRI with zero echo time. *eMagRes.* 2012;1:311-322.
16. Grodzki DM, Jakob PM, Heismann B. Ultrashort echo time imaging using pointwise encoding time reduction with radial acquisition (PETRA). *Magn Reson Med.* 2012;67:510-518.
17. Froidevaux R, Weiger M, Rosler MB, Brunner DO, Pruessmann KP. HYFI: hybrid filling of the dead-time gap for faster zero echo time imaging. *NMR Biomed.* 2021;34:e4493.
18. Weiger M, Overweg J, Rösler MB, et al. A high-performance gradient insert for rapid and short-T_2 imaging at full duty cycle. *Magn Reson Med.* 2018;79:3256-3266.
19. Rösler MB, Weiger M, Brunner DO, Schmid T, Froidevaux R, Pruessmann KP. An RF birdcage coil designed for an insert gradient coil dedicated to short-T_2 MRI. *Proceedings of the 25th Annual Meeting of ISMRM*. International Society for Magnetic Resonance in Medicine; 2017:2668.
20. Weiger M, Brunner DO, Dietrich BE, Muller CF, Pruessmann KP. ZTE imaging in humans. *Magn Reson Med.* 2013;70:328-332.

21. Schildknecht CM, Weiger M, Froidevaux R, Pruessmann KP. Rapid high power transmit-receive switching using a timed cascade of PIN diodes. *Proceedings of the 30th Annual Meeting of ISMRM*. International Society for Magnetic Resonance in Medicine; 2021:1411.

22. Rahmer J, Börnert P, Groen J, Bos C. Three-dimensional radial ultrashort echo-time imaging with T_2 adapted sampling. *Magn Reson Med*. 2006;55:1075-1082.

23. Schieban K, Weiger M, Hennel F, Boss A, Pruessmann KP. ZTE imaging with enhanced flip angle using modulated excitation. *Magn Reson Med*. 2015;74:684-693.

24. Bloom M, Burnell EE, Valic MI, Weeks G. Nuclear magnetic resonance line shapes in lipid bi-layer model membranes. *Chem Phys Lipids*. 1975;14:107-112.

25. Wennerström H. Proton nuclear magnetic resonance lineshapes in lamellar liquid crystals. *Chem Phys Lett*. 1973;18:41-44.

26. The Wellcome Centre for Human Neuroimaging. *Statistical Parametric Mapping (SPM) 12*. UCL Queen Square Institute of Neurology. Available at: https://www.fil.ion.ucl.ac.uk/spm/software/spm12/. 2020.

27. Tesiram YA. Implementation equations for HSn RF pulses. *J Magn Reson*. 2010;204:333-339.

28. Hargreaves B. Rapid gradient-echo imaging. *J Magn Reson Imaging*. 2012;36:1300-1313.

29. Wansapura Janaka P, Holland Scott K, Dunn RS, Ball WS. NMR relaxation times in the human brain at 3.0 tesla. *J Magn Reson Imaging*. 1999;9:531-538.

30. Richter D. *Neurochemistry*. Springer; 1980:1-64.

31. Dubal L, Wiggli U. Tomochemistry of the brain. *J Comput Assist Tomogr*. 1977;1:300-307.

32. Robertson C. Theory and practical recommendations for autocorrelation-based image correlation spectroscopy. *J Biomed Opt*. 2012;17:080801.

33. Nagel AM, Laun FB, Weber M-A, Matthies C, Semmler W, Schad LR. Sodium MRI using a density-adapted 3D radial acquisition technique. *Magn Reson Med*. 2009;62:1565-1573.

34. Ma Y-J, Jerban S, Jang H, Chang D, Chang EY, Du J. Quantitative ultrashort echo time (UTE) magnetic resonance imaging of bone: an update. *Front Endocrinol*. 2020;11:567417.

35. Godenschweger F, Kägebein U, Stucht D, et al. Motion correction in MRI of the brain. *Phys Med Biol*. 2016;61:R32-R56.

36. Ljungberg E, Wood TC, Solana AB, Williams SCR, Barker GJ, Wiesinger F. Motion corrected silent ZTE neuroimaging. *Magn Reson Med*. 2022;88:195-210.

37. Wilhelm MJ, Ong HH, Wehrli SL, et al. Direct magnetic resonance detection of myelin and prospects for quantitative imaging of myelin density. *Proc Natl Acad Sci*. 2012;109:9605-9610.

38. Pampel A, Müller DK, Anwander A, Marschner H, Möller HE. Orientation dependence of magnetization transfer parameters in human white matter. *Neuroimage*. 2015;114:136-146.

39. Holmes JE, Bydder GM. MR imaging with ultrashort TE (UTE) pulse sequences: basic principles. *Radiography*. 2005;11:163-174.

40. Nayak KS, Pauly JM, Gold GE, Nishimura DG. Imaging ultra-short T_2 species in the brain. *Proceedings of the 8th Annual Meeting of ISMRM*. International Society for Magnetic Resonance in Medicine; 2000:509.

41. Ercan E, Boernert P, Webb A, Ronen I. Whole-brain tissue-based assessment of the ultrashort T_2 component using 3D UTE MRI relaxometry. *Proceedings of the 20th Annual Meeting of ISMRM*. International Society for Magnetic Resonance in Medicine; 2012:4279.

42. Du J, Ma G, Li S, et al. Ultrashort echo time (UTE) magnetic resonance imaging of the short T_2 components in white matter of the brain using a clinical 3T scanner. *Neuroimage*. 2014;87:32-41.

43. Sheth V, Shao H, Chen J, et al. Magnetic resonance imaging of myelin using ultrashort Echo time (UTE) pulse sequences: phantom, specimen, volunteer and multiple sclerosis patient studies. *Neuroimage*. 2016;136:37-44.

44. Fan SJ, Ma Y, Zhu Y, et al. Yet more evidence that myelin protons can be directly imaged with UTE sequences on a clinical 3T scanner: bicomponent T_2* analysis of native and deuterated ovine brain specimens. *Magn Reson Med*. 2018;80:538-547.

45. Ma YJ, Searleman AC, Jang H, et al. Volumetric imaging of myelin in vivo using 3D inversion recovery-prepared ultrashort echo time cones magnetic resonance imaging. *NMR Biomed*. 2020;33:e4326.

46. Ma Y-J, Jang H, Wei Z, et al. Myelin imaging in human brain using a short repetition time adiabatic inversion recovery prepared ultrashort echo time (STAIR-UTE) MRI sequence in multiple sclerosis. *Radiology*. 2020;297:392-404.

47. Müller M, Egger N, Sommer S, et al. Direct imaging of white matter ultrashort T_2* components at 7 Tesla. *Magn Reson Imaging*. 2022;86:107-117.

48. Shen X, Özen AC, Sunjar A, et al. Ultra-short T_2 components imaging of the whole brain using 3D dual-echo UTE MRI with rosette k-space pattern. *Magn Reson Med*. 2023;89:508-521.

49. Seifert AC, Li C, Wilhelm MJ, Wehrli SL, Wehrli FW. Towards quantification of myelin by solid-state MRI of the lipid matrix protons. *Neuroimage*. 2017;163:358-367.

50. Seifert AC, Umphlett M, Hefti M, Fowkes M, Xu J. Formalin tissue fixation biases myelin-sensitive MRI. *Magn Reson Med*. 2019;82:1504-1517.

51. Jang H, Carl M, Ma Y, et al. Inversion recovery zero echo time (IR-ZTE) imaging for direct myelin detection in human brain: a feasibility study. *Quant Imaging Med Surg*. 2020;10:895-906.

52. Laule C, Vavasour IM, Kolind SH, et al. *Magn Reson Imaging Myelin*. *Neurother*. 2007;4:460-484.

53. Piredda GF, Hilbert T, Thiran JP, Kober T. Probing myelin content of the human brain with MRI: a review. *Magn Reson Med*. 2021;85:627-652.

SUPPORTING INFORMATION

Additional supporting information may be found in the online version of the article at the publisher's website.

Part 1. Simulations with noise.
Part 2. Fitted water map for M = 152 and no filter.
Part 3. Myelin bilayer map for another volunteer.